Article

Photonically active bowtie nanoassemblies with chirality continuum

 Check for updates

Prashant Kumar[1,2], Thi Vo[1,2], Minjeong Cha[1,2], Anastasia Visheratina[1,2], Ji-Young Kim[1,2], Wenqian Xu[3], Jonathan Schwartz[4], Alexander Simon[1], Daniel Katz[1], Valentin Paul Nicu[5], Emanuele Marino[6,7], Won Jin Choi[1,2], Michael Veksler[1], Si Chen[3], Christopher Murray[6], Robert Hovden[4], Sharon Glotzer[1,2,4 ✉] & Nicholas A. Kotov[1,2,4 ✉]

Chirality is a geometrical property described by continuous mathematical functions[1–5]. However, in chemical disciplines, chirality is often treated as a binary left or right characteristic of molecules rather than a continuity of chiral shapes. Although they are theoretically possible, a family of stable chemical structures with similar shapes and progressively tuneable chirality is yet unknown. Here we show that nanostructured microparticles with an anisotropic bowtie shape display chirality continuum and can be made with widely tuneable twist angle, pitch, width, thickness and length. The self-limited assembly of the bowties enables high synthetic reproducibility, size monodispersity and computational predictability of their geometries for different assembly conditions[6]. The bowtie nanoassemblies show several strong circular dichroism peaks originating from absorptive and scattering phenomena. Unlike classical chiral molecules, these particles show a continuum of chirality measures[2] that correlate exponentially with the spectral positions of the circular dichroism peaks. Bowtie particles with variable polarization rotation were used to print photonically active metasurfaces with spectrally tuneable positive or negative polarization signatures for light detection and ranging (LIDAR) devices.

Mathematical definitions of mirror asymmetry[1–5] recognize the continuity of chiral geometries that can be visualized by stretching macroscale helical springs to obtain coils of different lengths, that is, pitch. At smaller scales, continuously variable chirality can be observed for origami/kirigami sheets[7–9], nanocomposites[10,11] and polymeric solids whose shape and circular dichroism (CD) can be varied by external fields[12]. However, chirality in chemistry commonly manifests as a binary property: chiral molecules are either right- or left-handed and the descriptors for stereochemical configurations of enantiomers at molecular scale are correspondingly binary, for example D/L, R/S, M/P and Δ/Λ. The binary chirality of amino acids originates from a high-energy penalty for distorting the optical centre based on sp^3-carbon atoms. The discreteness of chirality in liquid crystals[13], macromolecular compounds[14], helical polymers[15] and nanoparticles (NPs)[16,17] manifests in abrupt transitions between chiral phases with different crystallinity or particle shapes[18]. Energy penalties are relaxed for large flexible molecules[19], supramolecular complexes[16,20,21] and biopolymers[18,22,23], but the restrictions on chiral shapes remain stringent. Unlike macroscale springs, the helical pitch across the variety of biomolecules varies little. For DNA, protein α-helices and β-sheets, pitch changes only in the ranges of 11–46, 2.3–5.5 and 7–8 Å, respectively; these narrow ranges are essential for the precise folding of biomolecules[24].

The transition from discrete chiral phases and shapes to a palette of chemical compounds with continuously tuneable chirality would be transformative for the development of chiral photonics, chiral metamaterials, biochemical separations and chiral catalysis. The availability of continuously variable chiral compounds is essential for establishing fundamental correlations between chirality measures and chemical properties. For example, the attempts to correlate optical activity with a variety of chirality measures have largely failed[25,26], but they could be possible for chiral nanostructures and their assemblies due to the differences in physics of chiroptical activity in them compared to molecules with binary chirality

Continuously variable chiral geometries become possible for nanostructured microparticles with bowtie shapes. They are hierarchically assembled from nanoribbons containing helical chains of cystine (CST, dipeptide of cysteine through the S–S bridge) interconnected by Cd^{2+} ions. The balance between short- and long-range interactions and defect tolerance of the electrostatically restricted assembly process[27] enables the synthesis of bowties with widely tuneable pitch, width, thickness and length.

Bowtie synthesis and structure

Mixing an aqueous solutions of Cd^{2+} and L- or D-cystine (Supplementary Fig. 1a,b) results in bowties (Methods) with pitch (p), width (w), thickness (t) and length (l) of 4.1, 1.3, 0.5 and 3.1 µm, respectively (Fig. 1a). The process is 100% enantioselective with L- and D-CST resulting in

[1]Department of Chemical Engineering, University of Michigan, Ann Arbor, MI, USA. [2]Biointerfaces Institute, University of Michigan, Ann Arbor, MI, USA. [3]X-ray Science Division, Advanced Photon Source, Argonne National Laboratory, Lemont, IL, USA. [4]Department of Materials Science and Engineering, University of Michigan, Ann Arbor, MI, USA. [5]Pro-Vitam Ltd, Sfantu Gheorghe, Romania. [6]Department of Chemistry, University of Pennsylvania, Philadelphia, PA, USA. [7]Department of Physics and Chemistry, University of Palermo, Palermo, Italy. ✉e-mail: sglotzer@umich.edu; kotov@umich.edu
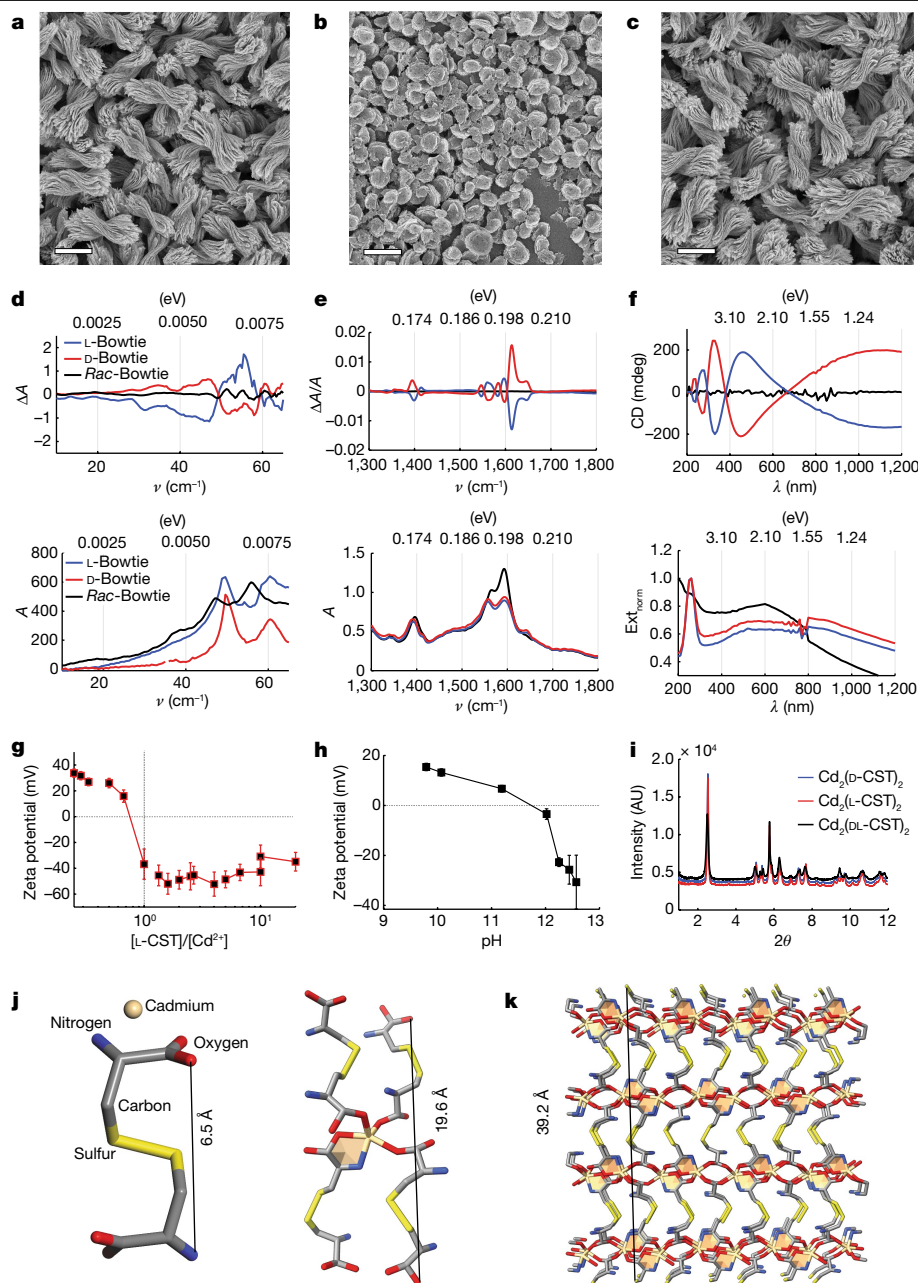
Fig. 1 | Hierarchical chirality from angstroms to micrometres via nanometers.
a–c, SEM images of bowties formed from Cd^{2+} and L-CST (left) (**a**), *rac*-CST (middle) (**b**) and D-CST (right) (**c**). Scale bars, 2 μm. **d–f**, CD (top) and extinction spectra (bottom) in THz (**d**), mid-IR (VCD) (**e**) and UV-visible-NIR (**f**) ranges for bowtie particles. **g**, Zeta potential of fully formed bowties at different ratios of L-CST and Cd^{2+} ions. **h**, Zeta potential of bowties formed from L-CST solution at different pHs. **i–k**, Synchrotron XRD pattern (**i**) and the calculated crystal structure of nanosheets (**j**) and nanoplatelets (**k**) forming the bowties. AU, arbitrary units. The unit cell is shown in Supplementary Fig. 6.

correspondingly left- and right-twisted bowties (Fig. 1a,c, and Supplementary Video 2); they are uniform in shape, size and handedness with standard deviation in *p*, *w*, *t* and *l* of 19.0, 13.6, 11.9 and 11.5%, respectively. Monodispersity of the bowtie particles indicates that they are formed in a self-limited assembly process (Supplementary Fig. 14)[5,6]. Nanostructured microparticles resembling a stack of flat nanoscale 'pancakes' are observed for *rac*-CST (Fig. 1b).

Electron microscopy, X-ray diffraction (XRD) and electron diffraction show levels of hierarchical organization within the cadmium cystinate bowties (Figs. 1i and 2a). Scanning electron microscopy (SEM) images for the terminal (Fig. 1a–c) and intermediate (Fig. 2a,b) stages of the synthesis show that bowties are structured as a stack of twisted

nanoribbons 200–1,200 nm in length and 45 nm in thickness (Supplementary Video 1). The nanoribbons are assembled from nanoplatelets 50–200 nm in length (Fig. 2c,d) and a thickness of roughly 1.2 nm calculated from the solved crystal structure (Supplementary Table 1, Supplementary Fig. 6 and Fig. 1k). Structural data in Supplementary Fig. 12 indicate that the nanoplatelets are formed from nanoclusters 1–2 nm in thickness, which is consistent with the thickness of the nanoplatelets and previous studies[28]. The nanoribbons and bowties acquire progressively stronger twists as the enantiomeric excess (±χ) of L- or D-CST increases (Fig. 2f).

Synchrotron XRD patterns helps in understanding how the atomic structure of bowties can accommodate their continuous changes in
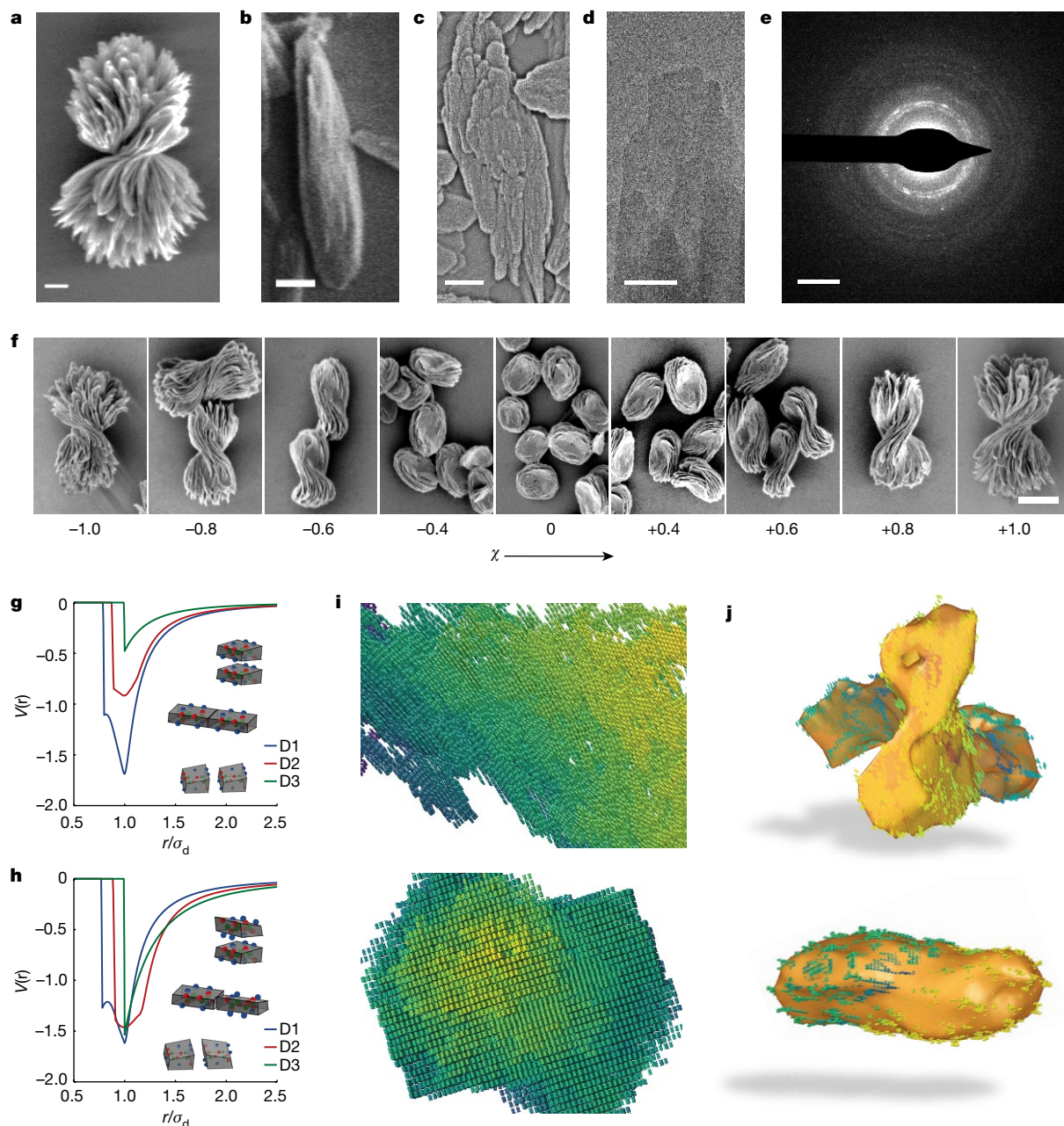
Fig. 2 | Non-binary chirality. a,b, SEM image of a fully formed bowtie (**a**), composed of twisted segments that are assembled from nanoribbons (**b**). **c**, SEM image of nanoribbons composed of polydisperse nanoplatelets. **d**, TEM image of the platelet. **e**. cryo-SAED pattern of the nanosheet in **d**. **f**, SEM images of the bowtie particles obtained by mixing different ratios of L-CST and D-CST, as defined by the enantiomeric excess (χ) show the transition from left-handed to pancake to right-handed bowties. Potentials of mean force obtained for preferred directions of interaction between two basic clusters of two permutations of chirality in CST ligands. **g,h**, LCL–LCL (**g**) and LCD–LCD (**h**) are computed and used for Monte Carlo growth simulations. The coarse-grained particle shapes deduced from the atomic structure of the nanocluster with the hydrogen bonding interaction sites marked by the spheres in LCL and LCD type nanoclusters are shown. **i,j**, Magnified snapshots from Monte Carlo simulations of the fully formed petal shows mismatched domains with local crystalline order arranged to form a twisted nanoribbon (**j**, top) and pancake type (**j**, bottom) petal for LCL (**i**) and LCD (**j**) type nanoclusters, respectively. Colour coding in **i** is only for visualization purposes. Scale bars, **a**, 1 μm; **b**, 0.5 μm; **c**, 200 nm; **d**, 100 nm; **e**, 2 nm^{-1} and **f**, 2 μm.

chirality while remaining chemically stable (Fig. 1a–c). Solving for the atomic structure followed by Rietveld refinement suggested several Cd-CST polymorphs (Supplementary Fig. 5–8 and Supplementary Table 1). Cumulative analysis of the XRD models points to Cd_2CST_2 nanoclusters (Fig. 1j) as the structural units of nanoribbons (Supplementary Fig. 8). These units produce helical chains (Fig. 1j,k and Supplementary Fig. 8) enabling partial swapping of L-CST for D-CST without drastic disruption of the short-range coordination bonds. The amine and carboxylic groups located on the exterior of the helical

chains form hydrogen bonds with neighbouring chains stabilizing the structure and facilitating the nanosheet stacking (Figs. 1j,k and 2c,d). A peak overlap below 2.5 Å in the XRD data indicates imperfections in atomic organization of nanosheets that are necessary for the chemical structure to produce a multiplicity of twisted shapes.

The reasons for variable chirality are encoded in the nanoscale building blocks. First, flexible hydrogen bonds allow for variable bond angles[17,18]. Second, the ability of nanoribbons to ionize (Fig. 1g,h) leads to the long-range repulsive interactions between nanoscale building

blocks that can be tuned over a wide range by changing the pH and ionic strength[29]. Because the nanoribbons twist, the electrostatic interactions are chiral, which reinforces the handedness of their assemblies. Geometric frustrations and related mechanical deformations are contributing factors, too. In case of nanoribbons, they leed to preferential geometries at atomic, nanometer, and submicron scales[17,28,30,31], which can be captured by microscale chirality vectors, Ξ (see below).

Selected-area electron diffraction (SAED) from a single nanoribbon confirms the XRD structural analysis (Fig. 2e). Cryo-SAED patterns are consistent with corresponding distances between planes in the orthorhombic Cd_2CST_2 structure (Supplementary Fig. 11). The nanoribbons are polycrystalline with ordered domains of helical chains appearing as sharp spots in the SAED pattern (Fig. 2e and Supplementary Fig. 17). Some degree of polycrystallinity enables the nanoribbons to accommodate CST ligands of opposite chirality while retaining the physical integrity of the nanoassembly. 'Imperfections' and variability of nanoribbon lengths is essential for the formation of such complex particles with continuously variable twisted shape.

Multispectral photonic activity

Extinction and CD spectroscopies from ultraviolet to terahertz (THz) frequencies demonstrate a rich set of mirror symmetric bands for the left- and right-handed bowties, whereas the 'pancake stack' assemblies are chiroptically silent (Fig. 1d,f). Visible light, Raman, Fourier transform infrared, mid-infrared and THz spectra (Fig. 1d–f) confirm the molecular structure of the bowties established by XRD and SAED. Peaks at 510 cm^{-1} in Raman spectra correspond to S–S disulfide stretches (Supplementary Fig. 2a). The strong and wide band from 3,000 to 3,750 cm^{-1} in Fourier transform infrared spectra confirms the multiplicity of hydrogen bonds stabilizing nanoribbons and their stacks. The CD spectrum has several positive and negative peaks denoted as P1 (−, 1,040 nm), P2 (+, 460 nm), P3 (−, 330 nm), P4 (+, 270 nm) and P5 (−, 235 nm) (Fig. 1f). P5 and P4 in the ultraviolet (UV) part of the spectrum are attributed to electronic transitions in the CST ligands. These two peaks are broadened and red-shifted compared to free CST due to coordination with Cd^{2+}. The vibrational CD (VCD) spectra of bowties and free CST are very different between 1,550 and 1,650 cm^{-1} (Fig. 1e). The former is 100 times more intense and contains many split bands. Density functional theory calculations (Supplementary Figs. 9 and 10) identified these bands as two carbonyl stretching modes (out-of-phase and in-phase modes) coupled with H-N-H scissor oscillations. These delocalized modes with long-range couplings between the helical chains in the nanoribbons result in large absorption cross-section and drastic increase in the intensity of 1,610–1,620 cm^{-1} band. The non-equivalency of the O atoms bonded to a Cd atom removes the degeneracy of the out-of-phase and in-phase modes resulting in band splitting (Figs. 1j,k and Supplementary Fig. 6). THz CD shows the existence of chiral phonons propagating along the nanoribbons (Fig. 1d)[32,33]. These data also indicate that the bowties made with L- or D-CST are true multiscale enantiomers of each other for which the mirror asymmetry is present at the subnanometre, nanometre and micrometre scales (the multiscale chirality vector below).

Computational models

On the basis of the solved crystal structure and zeta-potential measurements (Fig. 1g,h and Supplementary Figs. 20–22), we constructed a coarse-grained version of the basic nanocluster (Supplementary Fig. 13) (Methods). A Monte Carlo growth algorithm was used to simulate bowtie assembly from nanoclusters with an average net charge of +1. Because the addition of each new nanocluster increases the total charge of the growing particle, the self-assembly process is electrostatically restricted[32], with each extra nanocluster having to overcome an increasingly repulsive energy barrier. Computation of the pair-wise potentials (Fig. 2g,h) between L-homochiral and racemic versions of the

nanoclusters, abbreviated to L-CSTs (LCL) and LCD, revealed growth directions along which the nanoclusters anisotropically interact through hydrogen bonds that reflect the structural hierarchy. Nanoclusters assemble into nanoplatelets that grow into nanoribbons that stack to form the bowties. As the number of building blocks in the assembly increases, the size of the ordered domains in the nanoribbons also increases (shown in colour in Fig. 2i and Supplementary Fig. 15). The growth of nanoribbons stops when the net charge repulsion on the particle becomes sufficient to prevent further attachment of nanoclusters (Supplementary Fig. 36), balancing out the attractive forces. LCL nanoclusters form a twisted platelet (Fig. 2j, top row), whereas LCD nanoclusters form a flat sheet (Fig. 2j, bottom row). The model combining both electrostatic and geometric reconstructions correctly predicts the relationship between the enantiomeric composition of the nanoclusters, χ, and the chirality of the bowties propagating up in scale as the particles evolve in size. The long-range electrostatic restrictions combined with efficacy of multiscale chirality transfer for different χ results in the uniform pitch and size of the bowties (Fig. 2f and Supplementary Fig. 31). The evidence of the elastic stress in the stacks contributing to the hierarchical twist can be appreciated by the partial unwinding of the nanoribbons on disassembly of the bowties (Supplementary Fig. 18).

Tuneable chirality

Hierarchical assembly from chiral nanoclusters enables wide-range tuning of long- and short-range interactions by changing various physical–chemical parameters (Supplementary Fig. 25), which can be exemplified by three synthetic cases. In case 1, the increase of ionic strength results in the increase of l, w and t because the range of electrostatic interactions is reduced for high ionic strengths (Supplementary Fig. 20). In case 2, the zeta potential increase with pH results in the increase of l, w and t. De-protonation of the –COOH groups on the surface of nanoribbons and nanoplatelets results in the reduction of hydrogen bonding between the ribbons and, thus, in greater separation between the nanoribbons (Supplementary Figs. 21 and 22). In case 3, an increase of L-CST/Cd leads to an increase of l, w and t due to adsorption of the counter ions on the bowtie surface (Supplementary Fig. 16a). The increase of the CST concentration promotes (Fig. 3a and Supplementary Figs. 20 and 26) the close-range hydrogen bonding between the nanoclusters, resulting in thicker and wider nanoribbons (Fig. 3a and Supplementary Fig. 24).

The variability of the pitch serves as a demonstration of the tuneable chirality of these particles (Supplementary Fig. 33). The computational model describing the hierarchical self-assembly of the bowties from nanoclusters with intermediate formation of nanoplatelets and nanoribbons quantitatively predicts their geometry (Supplementary Figs. 31, 24 and 35). It also captures the variations of the geometrical parameters of the bowties in response to variations of ionic screening, solvents, enantiomeric excess, temperature and counter ions (Fig. 3d,e and Supplementary Figs. 25–33 and 39–43).

The chirality continuum can be demonstrated by calculating chirality measures, such as Hausdorff distance[1], continuous symmetry measure[2] or Osipov–Pickup–Dunmur (OPD) index (Supplementary Information)[3]. All of them are suitable for establishing the variable chirality of the bowties, but OPD has an additional useful feature: it changes sign when switching from left to right enantiomers. The transition from discrete to continuous chirality is evident from Fig. 3d,e because the pitch and OPD cover a wide range of values. For example, standard OPD varies gradually from −4.7 to +4.6, whereas other molecular or nanoscale systems have only discrete points (Fig. 3d).

Nanoassemblies have chirality at many levels, which is essential for establishing the properties of chemical structures displaying chirality continuum. Multiscale chirality can be expressed as a chirality vector $Ξ(ξ_1,ξ_2,ξ_3,ξ_4...)$ where components $ζ_i$ represent chirality
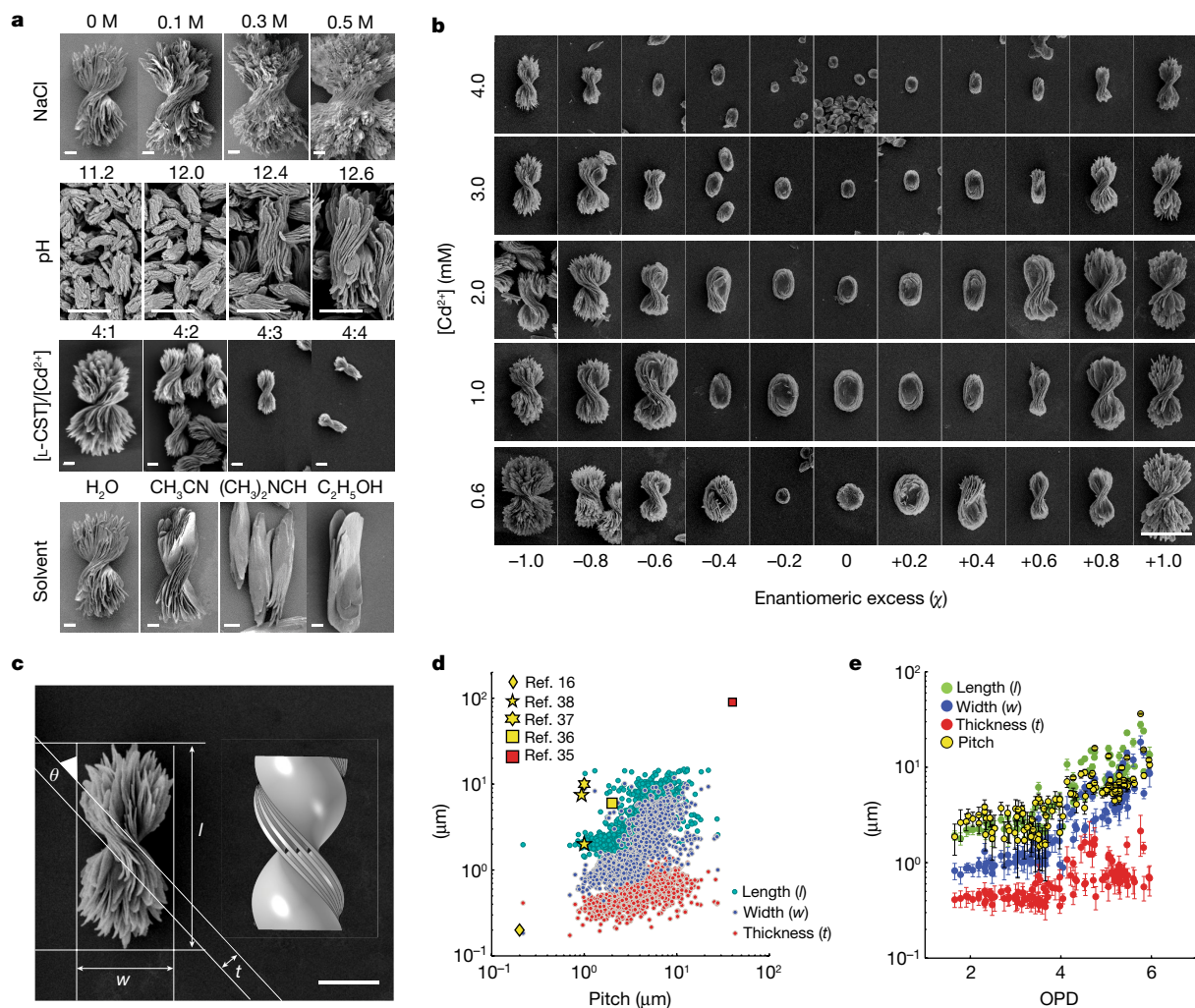
Fig. 3 | Morphological diversity of bowties. a, Effect of NaCl, pH, excess charge (L-CST/Cd), solvent (1:1 water to solvent) on bowtie morphology (water, [Cd^{2+}] = 1 mM, 4 mM for pH, [L-CST] = 4 mM) are shown. Scale bar, 1 μm. **b**, Continuously variable twist and sizes for bowtie particles obtained for different χ and [Cd^{2+}]. Scale bar, 5 μm. **c**, SEM image of a typical bowtie assembly and the corresponding morphological parameters of length (l), width (w), thickness (t) and pitch ($2w\tan(90 - \theta)$) overlaid. Three-dimensional models (right) used in computations of OPD chirality measures. Scale bar, 2 μm. **d**, Scatter chart demonstrating the variability of the geometrical parameters (l, w, t) versus pitch (p) for the bowtie assemblies obtained in this study and the same parameters obtained in other studies[16,36–39]; bowties retain their shape over two orders of length scales. **e**, Variation of the morphological parameters with calculated OPD chirality measure show empirical correlations between the l, w, t, p and OPD.

measures at specific scales. For example, $\Xi_{bowties}$ will comprise OPD for CST ligands, constituent nanoclusters, individual nanosheets (Fig. 1j,k) and bowties overall (Fig. 2a), resulting in $\Xi(\xi_i) = \Xi(-1.1 \times 10^{-3}; 1.4 \times 10^{-2}; 6.81 \times 10^{-4}; 2.75 \times 10^{-2})$; as all of them have different numbers of points, the point-scaled chirality measure OPD$_s$ instead of standard OPD was used. For some components, i.e. ξ_1, chirality continuum is not observed, but for the level of fully assembled particles it is and is being considered henceforth.

Testing the correlation between the sign of peaks in the CD spectra (Figs. 3e, 4a and Supplementary Fig. 47d,e) is fundamentally important because of the long-standing controversy about the suitability of sign-changing pseudoscalar measures of chirality for the description of experimental data[5,34]. We found that the sign of OPD correlates with the experimental CD spectra, g-factor spectra and P3, P2 and P1 peaks (Fig. 4a and Supplementary Figs. 49 and 50)[5,34]. An exponential relationship between OPD and the spectral position of the P2 and P3 peaks was observed (Fig. 4c). We note that organic and biological chemistries do not provide, hitherto, examples of quantifiable property–chirality relationships, despite extensive discussions of their possibility[4,5,25,35].

Bowtie-based photonic materials

Experimental dependences of P2/P3 peaks versus OPD indicate that the physical laws governing chirality–property relationships for nanostructured microparticles and small molecules are different. We found that the computational models describing bowties as a stack of twisted ribbons accurately explain the signs and red-shifts of P3, P2 and P1 peaks across the entire parameter space (Fig. 4a–e and Supplementary Figs. 25, 27, 28, 39–43 and 45). Decomposition of the extinction spectra from right-handed bowties into scattering and absorptive components showed that the negative P3 and P1 peaks and positive P2 peak in Fig. 1f and Fig. 4a are from differential scattering (Supplementary Fig. 49). The computational predictions for peak position match experiments nearly perfectly (Fig. 3a,b and Supplementary Figs. 26, 27, 45 and 48–50). Electromagnetic field distributions indicate that P1 and P3 originate from a mix of dipolar and quadrupolar resonance scattering modes (Fig. 4a–h and Supplementary Fig. 54). Although the peak positions vary with particle size, the attribution of the peaks remains the same for all l, w, t and θ, as demonstrated by
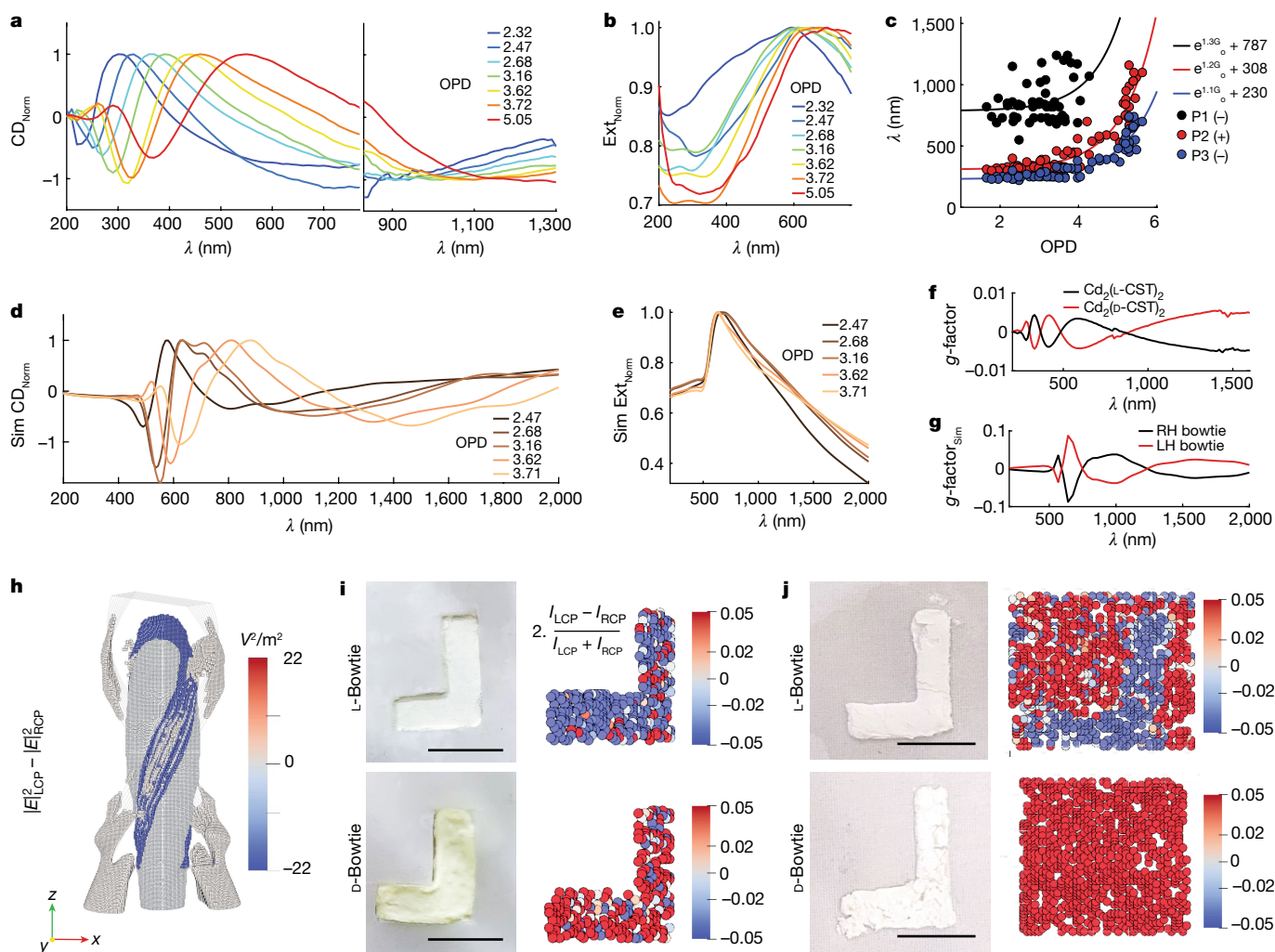
Fig. 4 | Optical properties of the bowtie particles. a, Normalized CD spectra for right-handed bowties of different OPD with peaks P1(−), P2(+), P3 (−) labelled. **b**, The corresponding extinction spectra. **c**, Dependences of spectral position of P1, P2, P3 with OPD made with varying [L-CST]/[Cd²⁺]. For peak P1, the dependence of its position on chirality measures is difficult to assess due to its breadth. **d,e**, Calculated g factor (**d**) and extinction (**e**) spectra are shown here for the right-handed twisted bowtie models with OPD values as in **a** and **b**. **f**, The g-factor spectra obtained for bowties prepared in an water-acetonitrile mixture with a peak at a 1,550 nm wavelength. **g**, Simulated g-factor spectra averaged for a bowtie model with l, w, t and θ as $5.3 \pm 0.3\,\mu m$, $2.1 \pm 0.1\,\mu m$, $0.7 \pm 0.1\,\mu m$, $46 \pm 5°$ along 25 different orientations with respect to an incident electromagnetic wave. **h**, Spatial distribution of differential ($|E|^2_{LCP} - |E|^2_{RCP}$) field around a bowtie model described in **g** shows enhancement of field within the layers. **i,j**, Printed coatings of 1.5×1.5 cm² L- and D-bowties on glass (**i**) and cloth (**j**) with the point-cloud of scattered signal on illumination with 1,550 nm wavelength chiral-LIDAR laser. Scale bar, 1 cm.

the calculations for the different models (Supplementary Figs. 49 and 50). Note that both scattering and absorption peaks of bowties involve the interaction of photons with the particle as a whole, not specific quantum states, which is essential for understanding the origin of observed chirality–property relationships (Fig. 4a–e). Optical properties of molecules originate from chiral shapes of molecular orbitals that may or may not correlate with the geometry of the sp^3 carbon atom or Δ/Λ enantiomers. Therefore, the similarity of the physical dimensions of chiral objects in bowties and incident photons engenders the observed dependences (Fig. 4c) and, thus, the fundamental difference in chirality–property relationships in comparison with small molecules, polymers and so on.

The simplicity of bowtie synthesis and the predictive relationship between particle structure and optical properties opens the door to the engineering of particle-based metasurfaces. We demonstrate that bowties can be used as templates for inducing chiroptical emission from achiral perovskite nanocrystals (Supplementary Fig. 51).

Coatings with circular polarization signatures (Supplementary Fig. 53) are needed for machine vision systems to increase the accuracy of object identification (for example, pedestrians). Dispersions of bowtie particles with strong circularly polarized P1 peak scattering in the near infrared (NIR) part of the spectrum were printed on glass slides and cotton fabric. A LIDAR operating at 1,550 nm with a circularly polarized beam (Supplementary Fig. 52) was used to acquire images of the printed objects following their decomposition into left- and right-handed components of back-scattered light originating from the P1 peak in CD spectra (Fig. 1f). The distinct contrast between prints made from the left- and right-handed bowties was observed (Fig. 4g and Supplementary Figs. 54–56). The layer of left-handed bowties can also be identified with high contrast on cotton cloth in LIDAR images (Supplementary Fig. 53d,e), which can be used in autonomous vehicles and other robots for the identification of specific materials and surface features exemplified by the polarization contrast from the micrometre-scale chirality of the fabrics and bowties.

Article

Dispersions of bowties translate into an emerging opportunity for scalable manufacturing of printable metasurfaces. The observed continuous correlations between the position of CD peaks and OPD indicate chirality–property correlations with pseudoscalar chirality measures arise when simple chiral shapes continuously transition from left- to right-handed enantiomers through an achiral state of flat sheets by gradual twisting. Conversion of Cd-CST bowties into similarly shaped CdS particles and coating of bowties with a perovskite nanolayer (Supplementary Fig. 51) indicates that several other materials can be prepared with the same diversity of morphology (Supplementary Fig. 12). Besides machine vision, dipolar and quadrupolar photonic resonances enable chirality-based engineering of composite materials for chemical and biomedical technologies.

Online content

Any methods, additional references, Nature Portfolio reporting summaries, source data, extended data, supplementary information, acknowledgements, peer review information; details of author contributions and competing interests; and statements of data and code availability are available at https://doi.org/10.1038/s41586-023-05733-1.

1. Buda, A. B. & Mislow, K. A Hausdorff chirality measure. *J. Am. Chem. Soc.* **114**, 6006–6012 (1992).
2. Osipov, M. A., Pickup, B. T. & Dunmur, D. A. A new twist to molecular chirality: intrinsic chirality indices. *Molec. Phys.* **84**, 1193–1206 (1995).
3. Zabrodsky, H. & Avnir, D. Continuous symmetry measures. 4. Chirality. *J. Am. Chem. Soc.* **117**, 462–473 (1995).
4. Rassat, A. & Fowler, P. W. Is there a 'most chiral tetrahedron'? *Chemistry* **10**, 6575–6580 (2004).
5. Harris, A. B., Kamien, R. D. & Lubensky, T. C. Molecular chirality and chiral parameters. *Rev. Mod. Phys.* **71**, 1745–1757 (1999).
6. Xia, Y. et al. Self-assembly of self-limiting monodisperse supraparticles from polydisperse nanoparticles. *Nat. Nanotechnol.* **6**, 580–587 (2011).
7. Choi, W. J. et al. Terahertz circular dichroism spectroscopy of biomaterials enabled by kirigami polarization modulators. *Nat. Mater.* **18**, 820–826 (2019).
8. Nguyen, M.-K. & Kuzyk, A. Reconfigurable chiral plasmonics beyond single chiral centers. *ACS Nano* **13**, 13615–13619 (2019).
9. Dey, S. et al. DNA origami. *Nat. Rev. Methods Prim.* **1**, 13 (2021).
10. Probst, P. T. et al. Mechano-tunable chiral metasurfaces via colloidal assembly. *Nat. Mater.* **20**, 1024–1028 (2021).
11. Kim, Y. et al. Reconfigurable chiroptical nanocomposites with chirality transfer from the macro- to the nanoscale. *Nat. Mater.* **15**, 461–468 (2016).
12. Miyajima, D. et al. Liquid crystalline corannulene responsive to electric field. *J. Am. Chem. Soc.* **131**, 44–45 (2009).
13. Ohta, E. et al. Redox-responsive molecular helices with highly condensed π-clouds. *Nat. Chem.* **3**, 68–73 (2011).
14. Ma, W. et al. Chiral plasmonics of self-assembled nanorod dimers. *Sci. Rep.* **3**, 1934 (2013).
15. Yashima, E. et al. Supramolecular helical systems: helical assemblies of small molecules, foldamers, and polymers with chiral amplification and their functions. *Chem. Rev.* **116**, 13752–13990 (2016).
16. Lee, H. E. et al. Amino-acid- and peptide-directed synthesis of chiral plasmonic gold nanoparticles. *Nature* **556**, 360–364 (2018).
17. Jiang, W. et al. Emergence of complexity in hierarchically organized chiral particles. *Science* **368**, 642–648 (2020).
18. Medina, D. D. & Mastai, Y. Chiral polymers and polymeric particles for enantioselective crystallization. *Isr. J. Chem.* **58**, 1330–1337 (2018).
19. Gingras, M. One hundred years of helicene chemistry. Part 3: applications and properties of carbohelicenes. *Chem. Soc. Rev.* **42**, 1051–1095 (2013).
20. Ma, W. et al. Chiral inorganic nanostructures. *Chem. Rev.* **117**, 8041–8093 (2017).
21. Aida, T., Meijer, E. W. & Stupp, S. I. Functional supramolecular polymers. *Science* **335**, 813–817 (2012).
22. Ho, R.-M. et al. Block copolymers with a twist. *J. Am. Chem. Soc.* **131**, 18533–18542 (2009).
23. Wang, H.-F. et al. Generalizing the effects of chirality on block copolymer assembly. *Proc. Natl Acad. Sci. USA* **116**, 4080 LP–4084089 (2019).
24. Ido, S. et al. Beyond the helix pitch: direct visualization of native DNA in aqueous solution. *ACS Nano* **7**, 1817–1822 (2013).
25. Petitjean, M. Chirality and symmetry measures: a transdisciplinary review. *Entropy* https://doi.org/10.3390/e5030271 (2003).
26. Buda, A. B., der Heyde, T. A. & Mislow, K. On quantifying chirality. *Angew. Chemie Int. Ed. English* **31**, 989–1007 (1992).
27. Kotov, N. A., Fendler, J. H. & Dekany, I. Layer-by-layer self-assembly of polyelectrolyte-semiconductor nanoparticle composite films. *J. Phys. Chem.* **99**, 13065–13069 (1995).
28. Tang, Z., Zhang, Z., Wang, Y., Glotzer, S. C. & Kotov, N. A. Self-assembly of CdTe nanocrystals into free-floating sheets. *Science* **314**, 274–278 (2006).
29. Nguyen, T. D., Schultz, B. A., Kotov, N. A. & Glotzer, S. C. Generic, phenomenological, on-the-fly renormalized repulsion model for self-limited organization of terminal supraparticle assemblies. *Proc. Natl Acad. Sci. USA* **112**, E3161–E3168 (2015).
30. Gao, C. et al. Electrostatic shape control of a charged molecular membrane from ribbon to scroll. *Proc. Natl Acad. Sci. USA* **116**, 22030–22036 (2019).
31. Miller, J. M. et al. Conformational switching of chiral colloidal rafts regulates raft–raft attractions and repulsions. *Proc. Natl Acad. Sci. USA* **116**, 15792–15801 (2019).
32. Choi, W. J. et al. Chiral phonons in microcrystals and nanofibrils of biomolecules. *Nat. Photonics.* **16**, 366-373 (2022).
33. Yeom, J. et al. Chiromagnetic nanoparticles and gels. *Science* **359**, 309–314 (2018).
34. Millar, G., Weinberg, N. & Mislow, K. On the Osipov–Pickup–Dunmur chirality index: why pseudoscalar functions are generally unsuitable to quantify chirality. *Mol. Phys.* **103**, 2769–2772 (2005).
35. Pelayo, J. J., Whetten, R. L. & Garzón, I. L. Geometric quantification of chirality in ligand-protected metal clusters. *J. Phys. Chem. C.* **119**, 28666–28678 (2015).
36. Shaw, L. A. et al. Scanning two-photon continuous flow lithography for synthesis of high-resolution 3D microparticles: erratum. *Opt. Express* **26**, 14718 (2018).
37. Chang, Y.-H., Jang, J.-W., Chang, Y.-C., Lee, S.-H. & Siao, T.-F. Gold nanohelices: a new synthesis route, characterization, and plasmonic E-field enhancement. *ACS Omega* **5**, 14860–14867 (2020).
38. Kaschke, J. & Wegener, M. Gold triple-helix mid-infrared metamaterial by STED-inspired laser lithography. *Opt. Lett.* **40**, 3986 (2015).
39. Yan, J. et al. Self-assembly of chiral nanoparticles into semiconductor helices with tunable near-infrared optical activity. *Chem. Mater.* **32**, 476–488 (2020).

Methods

Synthesis of bowties

Cadmium chloride ($CdCl_2$), 99.99% trace metals basis, L-CST, ≥98% (TLC), crystalline, D-CST, 98%, sodium hydroxide (NaOH) pellets >97% were purchased from Sigma-Aldrich. De-ionized water (18.2 mΩ cm⁻¹) was used for the preparation of stock solutions and aqueous dispersions. The 10 ml stock solutions of $CdCl_2$ (0.1 M), L-CST (0.1 M), D-CST (0.1 M) and NaOH (2.5 M) were prepared by dissolving the required amounts in de-ionized water. pH of CST stock solution was raised to 11 by adding 1 ml of 2.5 NaOH in 10 ml of solution. An immediate change in appearance was observed by the formation of a clear solution. Remaining solids were dissolved by mild sonication for 10 s. Bowties were synthesized by the mixing stock solutions of $CdCl_2$ and L-CST or D-CST in a 1:1 stoichiometric ratio in an aqueous media. Typical synthesis involved 20 µl of L-CST added to 960 µl of water followed by the addition of 20 µl of $CdCl_2$. The solution mixture was shaken vigorously until the dispersion turned milky, which is an indicator of the bowties' assembly process. After that, the mixture was kept still at room temperature for 15 min to ensure the completion of the self-assembly. The dispersion was subsequently centrifuged three times in de-ionized water at 6,000 rpm for 3 min. Final aqueous dispersion was stored at room temperature and used for further characterization and studies. Bowtie dispersions for coatings were prepared by mixing the freeze-dried powder in polyacrylic acid.

Electron microscopy

SEM samples were prepared by drop-casting 5 µl of aqueous dispersion on 1 × 1 cm silicon wafers (TedPella), following by drying at room temperature. This was followed by sputter coating a 5–10 nm film of gold on the wafer to avoid charging due to the electron beam. SEM measurements were performed in FEI Nova NanoLab Dual Beam SEM and FEI Helios Nanolab at 5 kV accelerating voltage and 0.4 nA beam current under secondary electron detection mode.

TEM samples were prepared by drop-casting 10 µl of aqueous solution on to a copper grid coated with holey carbon supported by a continuous carbon film (TedPella 01824). Bright-field TEM was performed on JEOL 2010 operating at 300 kV accelerating voltage and acquisition were done using Gatan OneView camera. Annular dark-field–scanning transmission electron microscopy (ADF–STEM) and STEM–energy dispersive X-ray spectroscopy measurements were performed on cold-FEG JEOL 3100R05 with Cs aberration correction operating at 300 keV. A HAADF detector was used to acquire Z-contrast images in which the intensity is proportional to the atomic number of the column over which the electron probe is placed. Diffraction experiments were acquired using Thermo Fisher Talos F200X operated at 200 keV equipped with a Gatan OneView camera. The Elsa (698) Gatan Cryo Holder cooled specimens down to roughly 93 K for low-temperature measurements.

STEM tomography

The synthesized bowtie particles were dispersed in water and drop cast using a micropipet onto a 3 mm copper TEM grid dried at room temperature. The TEM grid was an ultrathin (3 nm) carbon film with a large hexagonal mesh (100) to provide high specimen tilts without beam shadowing (Electron Microscopy Sciences). The tomographic tilt series were acquired using a Thermo Fisher Talos F200X operated at 200 keV as a scanning transmission electron microscope with a 10.5 mrad semiconvergence angle using a 36 and 165 mrad inner and outer semicollection angles for the ADF detector. The right-handed bowtie particles were acquired over a tilt range of −72° to +73° and left-handed bowtie particles specimen were acquired over a tilt range of −75° to +71° both with a +1° tilt increment. At each angle, ADF images of size 1,024 × 1,024 pixels were recorded with a dwell time of 4 µs and pixel size of 4.94 nm. The tomograms were reconstructed with the additive simultaneous iterative reconstruction technique for 150 iterations. The three-dimensional reconstructions were visualized by tomviz[40].

XRD

Synchrotron X-ray powder diffraction data (λ = 0.45192 Å) were collected at Beamline 17-BM at the Advanced Photon Source at the Argonne National laboratory. A freeze-dried powder sample of L-/D-/*rac*-bowties was loaded in a 1.0 mm diameter Kapton capillary tube, which was then measured using a VAREX XRD 4343CT amorphous silicon area detector in the Debye–Scherrer geometry.

Measurements of particle geometry

Length (l), width (w), thickness (h) and angle of twist (θ) as defined in Fig. 3c were measured using Jann5s or the measure tool from MATLAB central. A minimum of ten measurements were taken for each parameter and standard deviation (σ) was calculated and represented as percentage variation by following the equation error = $\frac{\sigma_x}{\underline{x}} \times 100$, where $x = l, w, h, \theta$ and $\underline{x}$ is the mean of corresponding values.

Finite-difference time-domain simulations of optical properties

The CD and g-factor spectra were calculated using a software package (Lumerical Solutions Inc.; www.lumerical.com/tcad-products/fdtd/). We used total-field scattered-field sources that surrounded the structure being modelled. Circularly polarized light was generated by positioning two total-field scattered-field sources along the same forward axis at a 90° angle and with a phase difference of either −90° for photons with left-handed polarization or 90° for photons with right-handed polarization. Two analysis groups using box power monitors monitored the absorption and scattering cross sections (extinction is the sum of absorption and scattering). The FDTD simulation region was defined by a larger box monitor with a stretched-coordinate perfectly matched layer and non-uniform mesh type. Frequency profile monitors were inserted in the total-field region to calculate electric field distribution in 3D. The refractive index for water is 1.33. Convergence tests with different mesh sizes were performed to determine the best balance between computational time restraints and simulation accuracy. Simulations were carried out for the bowties oriented with their long axis being parallel with the propagation direction (**k** vector) of photons. The 10 and 1 nm mesh sizes produced similar CD spectra; therefore, we used 10-nm mesh size for bowtie simulations presented in Supplementary Figs. 49, 50 and 54.

Chiroptical spectroscopy

CD measurements in UV-visible and NIR range were performed using JASCO J-1700 equipped with one photomultiplier tube detector in 200–800 nm range and two InGaAs NIR detectors in 800–1,600 nm range. Typical scanning parameters were as follows: scanning speed, 500 nm min⁻¹; data pitch, 0.1 nm; bandwidth, 5 nm (NIR bandwidth, 10 nm), digital integration time, 0.25 s and one accumulation. The anisotropy g factor was calculated according to the equation $g = \frac{CD}{32,980 \times abs}$, where CD is the signal obtained from CD/DC channel and abs is the absorbance calculated from ABS and DC channels of the spectrophotometer. CD spectra were stopped at wavelengths in which the high-tension voltage was greater than 800 V to avoid artefacts during acquisition.

Terahertz CD spectroscopy

The terahertz (THz) time-domain polarimetry system based on three linear polarizers was used to measure THz absorption and THz CD spectra[7]. We used calculations of Stokes parameters based on the E_x and E_y, the electric field in the x and y directions, respectively. THz absorptions were extracted from the equations used in ref. [7] after retrieval of phase from the transmission data. To eliminate linear birefringence effects from samples, highly concentrated mixture of bowtie powders

Article

with mineral oil was used. The reference sample is a quartz sandwich cell filled with mineral oil[32].

VCD spectroscopy

VCD measurements were performed on freeze-dried bowtie samples dispersed in heavy water (D_2O) at 33 mg ml^{-1} concentration. A 100 μl drop was sandwiched between two BaF_2 crystals separated by a 50 μm Teflon spacer. An MCT-V detector was used to acquire infrared and VCD data in the range of 2,000 to 850 cm^{-1} with a resolution of 4 cm^{-1} and a total of 100 and 500 accumulations, respectively. The sandwiched dispersion between BaF_2 crystals was rotated along the *a* axis coinciding with the direction of the beam at a constant speed to avoid settling of particles. Corresponding infrared and VCD were plotted as A and $\frac{\Delta A}{A}$, respectively, with exclusion of the 1,300 to 1,100 cm^{-1} range that corresponds to strong absorption from D_2O. The simulation of the VCD spectra was performed using the method described in the Supplementary Information.

Coarse-grained modelling of bowtie particles

We pick features consistent with XRD results to construct a coarse-grained building block for the nanoclusters. The key features we chose to adapt are (Supplementary Fig. 13) as follows. (1) Flat, rectangular prism-like building blocks with rough dimensions of $20 \times 10 \times 5$ commensurate with XRD nanoclusters. (2) H-bonding sites decorate the two largest and two smallest facets to reflect the bonding between the –COOH and –NH_2 groups. (3) The two intermediate facets show a directional interaction to capture the disulfide bridge formation intrinsic to CST. These interactions sites only interact with themselves. (4) Building blocks show a slight shear on one facet to enforce chirality of L-CST versus R-CST. (5) Isotropic charge–charge repulsion between Cd^{2+} atoms embedded inside the building block: each has a net charge of +1 to build in charge-driven, self-limiting behaviours. (6) All other surface sites not defined above show steric repulsion.

Potential of mean force and Monte Carlo growth simulation

Potential of mean force (PMF) values between nanoclusters are computed by adding together all interactions as a function of the centre-to-centre distance between nanocluster pairs and performing weighted averaging. The resulting PMFs between LCL highlight directional growth features that are commensurate with the hierarchy of structural formation observed in experiments (Fig. 2g). PMFs computed for a mix of L-CST and R-CST (LCD) conversely suggest a reduction in hierarchical structural formation and chiral propagation (Fig. 2h). We then use the computed PMFs to perform Monte Carlo growth simulations. Specifically, the well depth of each computed PMF plus the net charge–charge repulsion between the next nanocluster and growing structure are used as the input energy in the Metropolis algorithm. This enables Boltzmann weighted selection of the direction in which to place the next building block in the growing structure. Visualization of the growth simulation results confirm the formation of bowtie and pancake morphologies (Fig. 2i,j).

Data availability

The authors declare that the data supporting the findings of this study are available within the article and its supplementary information files. Source data are provided with this paper.

40. Levin, B. D. A. et al. Tutorial on the visualization of volumetric data using tomviz. *Micros. Today* **26**, 12–17 (2018).